WATER RESOURCES RESEARCH, VOL. 42, W08424, doi:10.1029/2005WR004593, 2006

Front dynamics of supercritical non-Boussinesq gravity currents

C. Ancey,[1] S. Cochard,[1] S. Wiederseiner,[1] and M. Rentschler[1]

Received 16 September 2005; revised 15 May 2006; accepted 26 May 2006; published 17 August 2006.

[1] In this paper, we seek similarity solutions to the shallow water (Saint-Venant) equations for describing the motion of a non-Boussinesq, gravity-driven current in an inertial regime. The current is supplied in fluid by a source placed at the inlet of a horizontal plane. Gratton and Vigo (1994) found similarity solutions to the Saint-Venant equations when a Benjamin-like boundary condition was imposed at the front (i.e., nonzero flow depth); the Benjamin condition represents the resisting effect of the ambient fluid for a Boussinesq current (i.e., a small-density mismatch between the current and the surrounding fluid). In contrast, for non-Boussinesq currents the flow depth is expected to be zero at the front in absence of friction. In this paper, we show that the Saint-Venant equations also admit similarity solutions in the case of non-Boussinesq regimes provided that there is no shear in the vertical profile of the streamwise velocity field. In that case, the front takes the form of an acute wedge with a straight free boundary and is separated from the body by a bore.

Citation: Ancey, C., S. Cochard, S. Wiederseiner, and M. Rentschler (2006), Front dynamics of supercritical non-Boussinesq gravity currents, *Water Resour. Res.*, *42*, W08424, doi:10.1029/2005WR004593.

1. Introduction

[2] There is a growing number of models inspired from shallow water (Saint-Venant) equations, which are used to describe time-dependent, free surface flows involving fluids with various rheological features. Essentially, these models are based on a set of hyperbolic partial differential equations that are obtained by integrating the mass and momentum balance equations across the flow depth. Typical examples include density currents [*Rottman and Simpson*, 1983], particle suspensions [*Parker et al.*, 1986], viscoplastic fluids [*Huang and Garcìa*, 1998], dry granular flows [*Savage and Hutter*, 1989], saturated granular fluids [*Iverson and Denlinger*, 2001], etc.

[3] Impediments to accurate numerical solutions for these equations are many and include the problem of front tracking and shock formation [*LeVeque*, 2002]. In this context, seeking analytical solutions is of great interest to test the robustness and accuracy of numerical methods. For shallow water equations, *Ritter* [1892] worked out a solution for the so-called dam break problem, where an infinite volume of fluid is suddenly released on a smooth horizontal plane. Earlier extensive work dates back to *Grundy and Rottman* [1985, 1986], who showed that the shallow water equations admit stable similarity solutions and used the phase plane formalism to construct solutions that are more general than Ritter's solution. *Gratton and Vigo* [1994] elaborated on this method to take shock occurrence and upstream boundary conditions into account. These seminal papers were devoted to planar inviscid Boussinesq gravity currents, i.e., currents for which the Reynolds number is sufficiently high for the viscous dissipation to be negligible, while the resistance action of the ambient fluid implies a Benjamin-like condition at the front (i.e., finite flow depth at the front). A number of flows in nature and in the laboratory belong to this class of flows [*Simpson*, 1997]. Subsequent work has extended these results by addressing the effects of shearing and frictional forces [*Daly and Porporato*, 2004; *Hogg and Pritchard*, 2004].

[4] The case of non-Boussinesq gravity currents has received far less attention. When a current is in a non-Boussinesq, high-Reynolds-number regime, the density mismatch between the current and the ambient fluid is so pronounced that the resisting effect of the ambient fluid becomes negligible and one expects that the Benjamin-like condition at the front no longer holds. Figure 1a shows a typical example of a non-Boussinesq current: this is a high-speed, dry snow avalanche. Its bulk density was approximately 150 kg/m^3 versus 1.3 kg/m^3 for the surrounding air; its velocity ranged from 20 to 25 m/s, and the flow depth was approximately 1 m, which led to a Reynolds number of the order of 3×10^5. Note that the front is wedge shaped and followed by a thin tail, which means that the flow depth is zero at the front. In contrast, dilute powder snow avalanches are in a Boussinesq regime and their front takes the form of a blunt nose, as shown in Figure 1b, which is consistent with a Benjamin-like condition [see also *Ancey*, 2004].

[5] In their analysis, *Gratton and Vigo* [1994] stated that the non-Boussinesq boundary condition (i.e., vanishing flow depth at the front) can be retrieved from the Boussinesq case by making the Froude number at the front tend to infinity. However, from a purely mathematical point of view, the boundary value problem remains ill posed since the only regular similarity solution vanishing at the front is

[1]School of Architecture, Civil and Environmental Engineering, École Polytechnique Fédérale de Lausanne, Lausanne, Switzerland.

0043-1397/06/2005WR004593$09.00

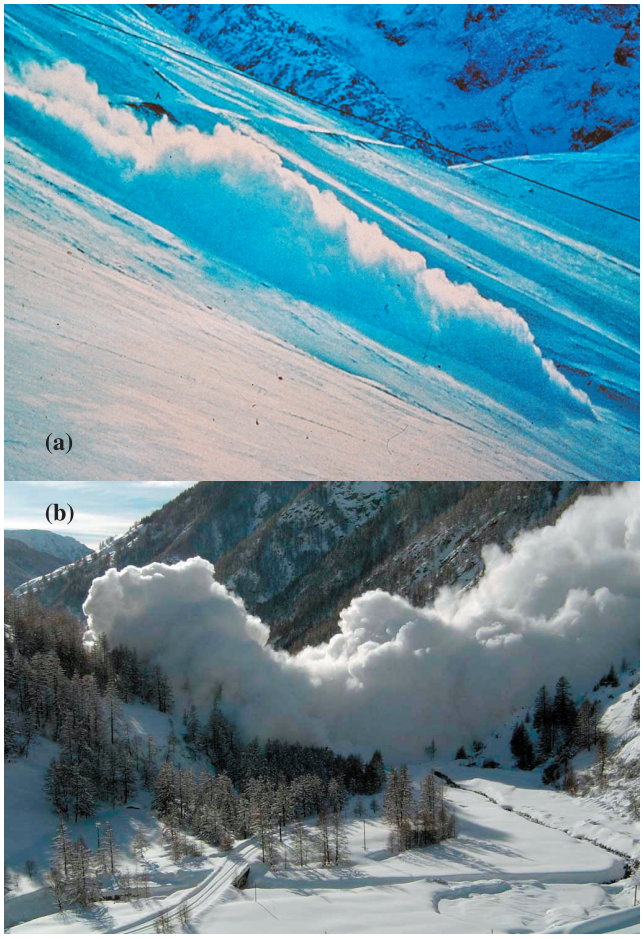

Figure 1. (a) Dry snow, high-speed, flowing avalanche in the experimental site of Lautaret Pass (France, courtesy of Cemagref). This avalanche is typical of a non-Boussinesq regime. (b) Power snow avalanche (Queyras, France, courtesy of Maurice Chave) in its runout phase. Air entrainment into the snow cloud induced a significant decrease in the bulk density, which led the avalanche to a Boussinesq regime.

the trivial solution (i.e., flow depth zero everywhere). From the physical standpoint, no clear justification or easy interpretation supports this statement. More recently, *Ruo and Chen* [2004] suggested that the boundary condition at the front is a part of the problem to be solved, but they were able to derive this condition solely for finite volume and constant inflow currents. *Montgomery and Moodie* [2001] modified the governing equations to transform them into an initial value problem. In the meantime, *Hogg and Pritchard* [2004] examined the Ritter solution to the dam break problem when the shallow water equations were slightly altered to take nonuniform velocity profiles (shearing effects) into account. Surprisingly enough, they discovered that it was not possible to locate the front position since the flow depth decreased toward 0 but never vanished.

[6] The objective of this paper is to examine the existence of similarity solutions for non-Boussinesq gravity currents when there is shear in the vertical profile of the horizontal velocity field and the current volume may grow as a power function of time. In this paper, we will revisit the paper by *Gratton and Vigo* [1994] and show that the proper solution associated with a zero flow depth at the front is a singular curve. We will also demonstrate that this curve exists only when the velocity is uniform within the tip region, which extends and supports the earlier conclusion of *Hogg and Pritchard* [2004].

2. Governing Equations

2.1. Flow-Depth-Averaged Equations

[7] We consider a shallow layer of fluid flowing over a rigid horizontal impermeable plane. The fluid is inviscid and incompressible; its density is denoted by ρ. The ratio $\epsilon = H_*/L_*$ between the typical vertical and horizontal length scales, H_* and L_* respectively, is assumed to be small. $U_* = O(\sqrt{gH_*})$ is the velocity scale.

[8] Integrating the local Euler equations over the flow depth provides the shallow water equations [*Stoker*, 1957; *Whitham*, 1974; *Chanson*, 2004]. The shallow water equations take the generic dimensionless form

$$\frac{\partial h}{\partial t} + \frac{\partial h\bar{u}}{\partial x} = 0,$$

$$\frac{\partial h\bar{u}}{\partial t} + \frac{\partial h\overline{u^2}}{\partial x} + h\frac{\partial h}{\partial x} = 0,$$

where the bar refers to flow-depth-averaged values, i.e., $\bar{u} = h^{-1}\int_0^h u(x, y, t)dy$, where $u(x, y, t)$ denotes the streamwise component of the local velocity field. The dimensionless velocity, flow depth, distance, and time were defined as $\bar{u} = \hat{u}/U_*$, $h = \hat{h}/H_*$, $x = \hat{x}/L_*$, and $t = \hat{t}U_*/L_*$, respectively, where the hat refers to dimensional variables. Introducing the Boussinesq coefficient γ makes it possible to relate the mean square velocity to the square of the mean velocity: $\overline{u^2} = \gamma\bar{u}^2$. The Boussinesq coefficient can be defined as

$$\gamma = 1 + \frac{1}{h}\int_0^h \left(1 - \frac{u(x,y,t)}{\bar{u}(x,t)}\right)^2 dy,$$

which shows that γ reflects the shear strength in the vertical profile of the horizontal fluid velocity. When $\gamma = 1$, there is no shear in the vertical profile of the streamwise velocity, whereas $\gamma > 1$ means that the velocity profile is sheared. Assuming that γ is known, we end up with a closed set of equations for h and $\bar{u}$

$$\frac{\partial h}{\partial t} + \frac{\partial h\bar{u}}{\partial x} = 0, \tag{1}$$

$$\frac{\partial \bar{u}}{\partial t} + (2\gamma - 1)\bar{u}\frac{\partial \bar{u}}{\partial x} + \bar{u}^2\frac{\partial \gamma}{\partial x} = -\frac{\partial h}{\partial x}\left(1 + \frac{\bar{u}^2}{h}(\gamma - 1)\right). \tag{2}$$

When γ is set equal to unity in the momentum balance equation (2), we retrieve the usual form of the shallow water equations [*Stoker*, 1957]. When γ is constant and in excess of unity, equations (1)–(2) are identical to the equations used by *Hogg and Pritchard* [2004] to analyze the effect of shear on front structure. In that case, the structure of the governing equations is slightly altered: the convective acceleration term

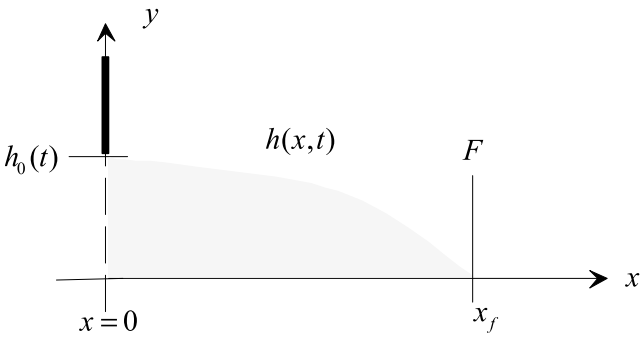

Figure 2. Configuration of the flow.

is weighted by the shape factor $2\gamma - 1$, while a Chézy-like term affects the pressure gradient. These modifications are minor and do not disturb the hyperbolic nature of the equations; they may, however, have significant impact on some occasions, e.g., when computing the nose features in the dam break problem [*Hogg and Pritchard*, 2004]. A pervasive assumption is to ascribe the Boussinesq coefficient to unity by advocating that in the high-Reynolds-number limit, the velocity profile is blunt, which implies that γ must not differ significantly from unity.

2.2. Flow Geometry and Boundary Conditions

[9] A two-dimensional flow regime is assumed, namely any cross-stream variation is neglected. The depth of the layer is given by $h(x, t)$ (see Figure 2). The flow is generated by a source of fluid: at $t = 0$, the sluice gate at the inlet is raised with a given aperture rate $h_0(t)$, specified below. Ahead of the front, there is a dry bed.

[10] At the source $x = 0$, the boundary condition is given by the relation

$$\bar{u}h = nAt^{n-1}, \tag{3}$$

which stems from imposing a given volume growth rate at the inlet

$$\mathcal{V} = \int_0^{x_f} h(x,t)dx = At^n,$$

with n a prescribed coefficient. According to *Gratton and Vigo* [1994], we must constrain n to lie within the range $0 \leq n < 4$; this condition on n is needed for the shallowness assumption to be consistent. We furthermore assume that the Froude number at the source is imposed: $Fr_0 = \bar{u}/\sqrt{h} = \alpha$, where α is a constant. The flow depth varies with time: $h = h_0(t) = \beta t^m$, where $m = \frac{2}{3}(n - 1)$ and β is another constant satisfying $\alpha\beta^{3/2} = nA$.

[11] The other boundary conditions are prescribed at the front. The front position x_f is the point where the flow depth drops to zero: $h(x_f) = 0$; moreover, the front velocity is $\bar{u}(x_f) = \dot{x}_f$.

2.3. Jump Conditions

[12] The solutions to the system (1)–(2) may admit discontinuities (called shock or hydraulic jump in the hydraulic literature). The flows either side of these are connected by jump conditions, which express conservation of mass and momentum across the moving discontinuity. Denoting the shock speed by σ, we can write these jump conditions associated with a conservative form of equations (1)–(2) as follows [*Whitham*, 1974]

$$[\![h\bar{u}]\!] = \sigma[\![h]\!], \tag{4}$$

$$[\![\gamma h\bar{u}^2 + h^2/2]\!] = \sigma[\![h\bar{u}]\!], \tag{5}$$

where the $[\![\cdot]\!]$ denotes the difference upstream and downstream of the shock.

3. Phase Plane Formalism

[13] In order to solve the similarity problem, we will use the phase plane (or portrait) formalism, as earlier authors did for the same kind of problem [*Grundy and Rottman*, 1986; *Gratton*, 1991; *Gratton and Vigo*, 1994]. The types and characteristics of the similarity solutions are described in detail by *Gratton and Vigo* [1994]. When the downstream boundary condition is of the Benjamin type, i.e., at the front, the Froude number is constant and the flow depth is nonzero, Gratton and Vigo claimed that the boundary condition $h(x_f) = 0$ is obtained asymptotically by making the Froude number tend to infinity [*Gratton and Vigo*, 1994], but we will show that in the particular case investigated here ($\gamma > 1$), their construction is not always possible. Except for this point, the formalism is identical to that used by *Gratton and Vigo* [1994] and we will not replicate their results here.

[14] *Gratton and Vigo* [1994] have shown that the governing equations (1)–(2) admit similarity solutions for a range of conditions at the source. Following *Grundy and Rottman* [1986] and *Gratton and Vigo* [1994], we pose

$$\bar{u} = \delta\xi t^{\delta-1} V(\xi),$$

$$h = \delta^2\xi^2 t^{2(\delta-1)} Z(\xi),$$

where we have introduced the similarity variable

$$\xi = \frac{x}{t^\delta},$$

with δ to be determined from the initial conditions (2), hence $\delta = (n + 2)/3$. The boundary conditions at the front impose

$$Z(\xi_f) = 0 \text{ and } V(\xi_f) = 1, \tag{6}$$

where ξ_f denotes the front position. The former condition $Z = 0$ is obvious; the latter one stems from the following relation: since the front point is a material point, its velocity is given by $\bar{u}_f = dx_f/dt$, which in terms of similarity variables, is equivalent to $V(\xi_f) = 1$. At the source, we have the asymptotic behavior

$$Z \propto \frac{\beta}{\delta^2\xi^2} \text{ and } V \propto \frac{\alpha\sqrt{\beta}}{\delta\xi} \text{ when } \xi \to 0. \tag{7}$$

Table 1. Properties of the Special Curves C_A, C_F, C_I, and C_J

Label	Equation	Properties
C_A	see equation (16)	exceptional solution to equation (9)
C_F	$F = 0$	integral path having horizontal tangent when crossing C_F
C_I	$Z = I(V)$	critical curve separating sub- and super-critical regimes
C_J	$Z = J(V)$	integral path having vertical tangent when crossing C_J

Since the solution may admit discontinuities, we supplement the following condition derived from equation (2), which ensures that the mass balance is not violated

$$\int_0^{\xi_f} \xi^2 Z(\xi) d\xi = \delta^{-2} A. \tag{8}$$

When there is not discontinuity, this equation is redundant with equation (7).

4. Similarity Solutions

[15] We shall see that ξ is an autonomous variable in the governing equations for Z and V, which means that we can get rid of ξ and directly seek a relation between Z and V by solving a first-order ordinary differential equation in the form

$$\frac{dZ}{dV} = \frac{F(V,Z)}{G(V,Z)}. \tag{9}$$

The behavior of the solutions to this equation can be qualitatively outlined by working in the V–Z plane and discussing the various possibilities of finding an "integral" curve passing through a given region.

4.1. Matrix Representation and Critical Curves

[16] Substituting the similarity forms into the governing equations (1)–(2), we obtain two ordinary first-order differential equations for Z and V that can be cast in a matrix form

$$\mathbf{M}(V,Z)\frac{d\mathbf{w}}{d\xi} = \frac{Z}{\delta\xi}\mathbf{S}(V,Z), \tag{10}$$

with $\mathbf{w} = [Z, V]^{\mathrm{T}}$,

$$\mathbf{M} = \begin{bmatrix} V-1 & Z \\ (\gamma-1)V^2 + Z & Z(V(2\gamma-1)-1) \end{bmatrix}, \text{ and}$$
$$\mathbf{S} = \begin{bmatrix} 2 - 3V\delta \\ V(1 - V(4\gamma-3)\delta) - 2\delta Z \end{bmatrix}.$$

This matrix form makes the discussion on the solution construction a bit easier. The determinant of the matrix $\mathbf{M}$ is

$$\det \mathbf{M} = \delta Z(Z - I(V)),$$

with $I(V) = 1 + (V - 2)V\gamma$. Along the V-axis ($Z = 0$) and the curve C_I of equation $Z = I(V)$, the solutions $V(\xi)$ and $Z(\xi)$ to equation (10) are not properly defined because det $\mathbf{M} = 0$: these functions are multivalued except when the crossing occurs close to a critical point. A multivalued behavior is not physically admissible and this issue is fixed by constructing discontinuous solutions (see Section 5). At a critical point, both $\mathbf{S}$ and $\mathbf{M}$ vanish and in that case, the crossing can be possible; the special solution $Z = \frac{1}{4}(9 - 8\gamma)V^2$ provides a typical example (see section 6.1 and equation (15)).

[17] When det $\mathbf{M}$ is nonzero, the system of equations (10) can be inverted to provide

$$\xi\frac{dZ(\xi)}{d\xi} = \frac{F(V,Z)}{\delta(Z - I(V))}, \tag{11}$$

$$\xi\frac{dV(\xi)}{d\xi} = \frac{G(V,Z)}{\delta(Z - I(V))}, \tag{12}$$

with $F(V, Z) = -Z(2Z\delta + V(-2V\delta\gamma + 4\gamma + 3\delta - 3) - 2)$ and $G(V,Z) = Z(2 - (V+2)\delta) + V(V(2\gamma + ((V-4)\gamma + 3)\delta - 3) + 1)$.

[18] Instead of solving this system of differential equations, we form the ratio of the two equations to arrive at a single ordinary differential equation (9) for $Z'(V)$. This allows us to work in the V–Z plane.

[19] When det $\mathbf{M}$ is zero, the system may have solutions if the determinant of the cofactor matrix

$$\mathbf{N} = \begin{bmatrix} V-1 & 3V\delta - 2 \\ (\gamma-1)V^2 + Z & 2\delta Z + V(V(4\gamma-3)\delta - 1) \end{bmatrix},$$

is also zero. In the space (V, Z), the locus of the points for which det $\mathbf{N} = 0$ is a continuous curve C_J of the equation

$$Z = J(V) = \frac{V(\gamma\delta V^2 + (-4\delta\gamma + 2\gamma + 3\delta - 3)V + 1)}{(V+2)\delta - 2}.$$

Note that $G(V, Z) = (2 - (V + 2)\delta)(Z - J(V))$, which means that C_J is also the locus of points where the integral curves have vertical tangents. Except for the case $\gamma = 1$ and $n = 1$ ($\delta = 1$), the curves C_I and C_J intersect at two points: A_γ with coordinates $(2/(4\gamma - 3), (9 - 8\gamma)/(4\gamma - 3)^2)$ and P_* with coordinates $(1, 1 - \gamma)$. P_* lies inside the first quadrant only when $\gamma \leq 1$. These points play an important role since their existence means that there may be continuous solutions with discontinuous gradients at points A and P_*. They will be useful thereafter in constructing the solutions (see Section 5). Note that the so-called dam break or Ritter problem is the particular case, where $\gamma = 1$ and $n = 1$ [*Whitham*, 1974]; in that case, the curves C_I and C_J coincide, which implies that a piece of this curve is a part of the solution sought.

4.2. Special Curves and Critical Points

[20] In addition to the curves C_I and C_J, there is another specific curve that plays a role in the phase portrait: the curve C_F is the curve along which F vanishes, i.e., at which the integral path has a horizontal tangent; its equation is given by

$$Z = \frac{2 + V(3 - 3\delta + 2\gamma(-2 + V\delta))}{2\delta}.$$

The properties of these curves are summarized in Table 1.

[21] In the first quadrant of the phase plane V–Z, there are three critical points resulting from the crossing of the

Table 2. Position and Properties of the Critical Points of Equation (9) Closest to the Front Point P[a]

Singular Points	Coordinates	K	Type
O	(0, 0)		node
A_γ	$\left(\frac{2}{4\gamma-3}, \frac{9-8\gamma}{(4\gamma-3)^2}\right)$	$K>0$ $K<0$	node saddle
B_γ	$\left(\frac{2}{3\delta}, \frac{9-8\gamma}{(3\delta)^2}\right)$	$K>0$ $K<0$	saddle node

[a]The behavior of points A and B depends on the sign of $K = (\delta - 1)(4\gamma - 3(1 + \delta))$.

specific curves C_F and C_J: there are also two other points resulting from the crossing of $Z = 0$ and C_J that we do not comment on here [see *Gratton and Vigo*, 1994, Table 1]. The first one is the origin point O. Point A_γ is also a singularity. The third one is referred to as point B_γ and has coordinates $(2/(3\delta), (9 - 8\gamma)/(9\delta^2))$. Table 2 summarizes the topological properties of the critical points A_γ, B_γ, and O depending on the sign of $K = (\delta - 1)(4\gamma - 3(1 + \delta))$.

[22] Figure 3 shows a few trajectories, the specific curves (C_I, C_J, and C_F), the critical points (O, A_γ, B_γ), the intersection point P_* between C_I (solid line) and C_J (dashed line), and the front P in the particular case $n = 5/2$ (the same as that shown in Figure 1 of Gratton and Vigo's paper). Note that at A_γ, the three curves C_I, C_J, and C_F meet, which implies significant behavior changes close to point A_γ. A few trajectories (thin curves with arrows) representing solutions to equation (9) are also reported and illustrate the behavior of the solutions close to the critical points; not all the paths are physically meaningful since some cross the critical curve C_I (solid line).

5. Flow Discontinuity

5.1. Rankine-Hugoniot Condition

[23] *Gratton and Vigo* [1994] computed the jump conditions differently from what is expounded here: they introduced the notion of conjugate curves stemming from hydraulics. In short, with each trajectory that lies in the subcritical part of the phase plane is associated a conjugate curve that lies in the supercritical region and represents the locus of points that satisfy the jump conditions with respect to the subcritical curve; finding the intersection of a trajectory and its conjugate leads to determining the end point of the continuous trajectory, marking the discontinuous transition to another state.

[24] Later, *Montgomery and Moodie* [2001] and *Hogg and Woods* [2001] used the jump conditions (4)–(5), with the only difference being that they expressed the conditions in the frame relative to the jump. Note that these two equations (4)–(5) involve three unknown variables, thus are not closed, contrary to the equations used by *Gratton and Vigo* [1994]. This implies that another condition is needed to compute the jump features.

[25] We shall see that this additional condition can be provided by the volume balance equation (8). The crossing of the critical curve C_I is not possible except when it occurs at point A_γ. When the crossing is not permitted, a shock occurs, which is ruled by the jump conditions (4)–(5). If we know the flow variables Z_1 and V_1 upstream (respectively, downstream) of the shock, we can solve the shock equations (4)–(5) to determine the shock velocity σ and a curve referred to as the shock curve $V_2(Z_2|Z_1, V_1)$, which is the locus of all the points satisfying the jump conditions (4)–(5). Solving this system of equations, we derive the shock velocity and the variation in upstream velocity V_2 with upstream flow depth Z_2

$$\sigma = \frac{\gamma}{\chi} V_1 \pm \frac{1}{\chi}\sqrt{\frac{1}{2}\left(\chi(Z_1+Z_2)+2(\gamma-1)V_1^2\right)\frac{Z_2}{Z_1}}, \tag{13}$$

$$V_2(Z_2|Z_1,V_1) = \frac{V_1}{\chi} \pm \frac{(Z_2-Z_1)}{\chi}\sqrt{\frac{1}{2}\frac{\chi(Z_1+Z_2)+2(\gamma-1)V_1^2}{Z_1Z_2}}, \tag{14}$$

with $\chi = \gamma + (1 - \gamma)\frac{Z_2}{Z_1}$. In the derivation of (13)–(14), we have assumed that the Boussinesq coefficient is the same either side of the jump. Similar albeit far more complicated relations can be derived when the jump is associated with a modification in the velocity profile; we will not report these relations here since they do not entail any change when we compute the shock from upstream to downstream (although the converse is not true). Since there is a quadratic dependence on velocity in equations (4)–(5), we actually find two shock curves, but a single one is physically admissible by requiring that energy dissipation through the shock be positive. This shock curve is then used to pass from one trajectory to another one that satisfies the boundary conditions downstream (respectively, upstream). The problem boils down to finding the point (V_1, Z_1) at which the shock occurs. To that end, we use a trial and error procedure: first we select a point (V_1, Z_1) on the integral path emanating from the source S, then we plot the shock curve $V_2(Z_2|Z_1, V_1)$, and finally we find the intersection point between the shock curve and the other integral path coming from the front point P. The procedure is iterated until the fluid volume found by numerical integration is consistent with the inflow rate imposed at the entrance (8). An example is provided below (see section 6.2).

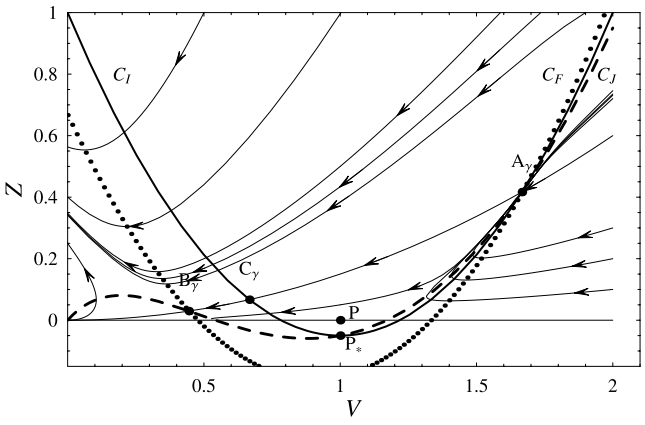

Figure 3. Specific curves C_I (solid line), C_J (dashed line), and C_F (dotted line). The thin curves with arrows represent a few trajectories computed numerically. The critical points O, A_γ, B_γ, and C_γ are plotted together with the front (point P). Computations are made for $n = 5/2$ and $\gamma = 1.05$.

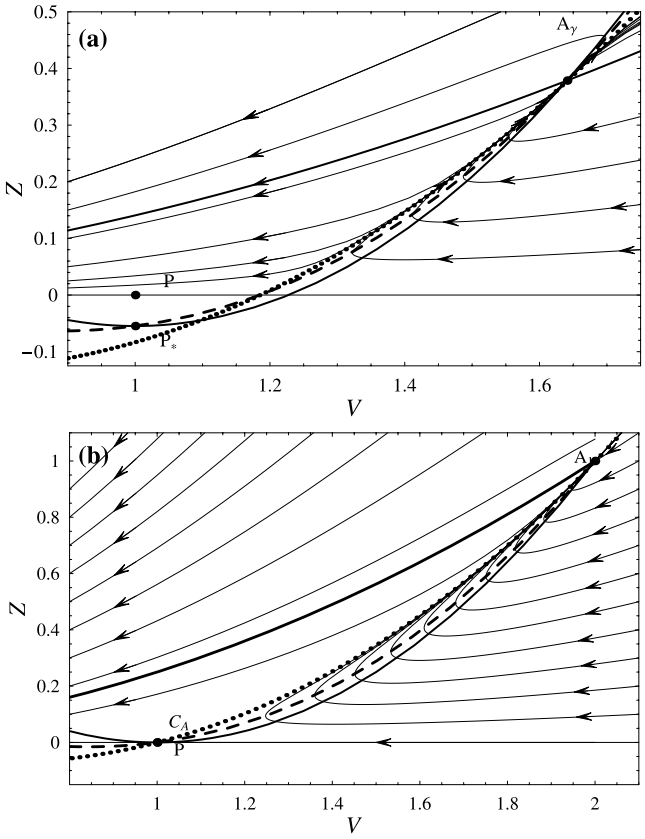

Figure 4. Specific curves C_I (solid line), C_J (dashed line), together with C_A (dotted line). (a) Computations made for $n = 5/2$ and $\gamma = 1.05$. (b) Computation made for $n = 5/2$ and $\gamma = 1$. The thin curves with arrows represent a few trajectories computed numerically; the arrows indicate increasing ξ. The critical point P_* is plotted together with the front P (they coincide in Figure 4b).

5.2. Weak Discontinuities

[26] It is worth recalling that a particular case of discontinuity includes the functions that are continuous, but whose derivative is not continuous at isolated points. This case is encountered when the curves C_I and C_J coincide (i.e., for $\gamma = 1$ and $n = 1$): when an integral curve crosses the critical curve, we have both det $\mathbf{M} = 0$ and det $\mathbf{N} = 0$, which implies that at this point, we can pass from one trajectory to another one and since det $\mathbf{N} = 0$, the new trajectory is a piece of C_I [see *Gratton and Vigo*, 1994, section 5.2].

6. Similarity Solutions for $\gamma > 1$

[27] We are interested in determining the solutions to equation (9) with $\gamma > 1$ and which evolve in the first quadrant ($V \geq 0$, $Z \geq 0$) and are related to boundary conditions (6)–(8). For a given set of upstream boundary conditions, the solution is represented in the phase plane by a curve referred to as $\mathcal{C}$, which links the source point S and the front point P. The boundary condition (7) implies that the source point S lies at infinity on $\mathcal{C}$. Point P has coordinates (1, 0) in this phase plane. Since we are interested in supercritical flows, the source point lies below the critical curve C_I and is associated with a Froude number in excess of unity (i.e., $\alpha > 1$). The front point P always lies in the subcritical region, which means that a weak or strong shock must occur.

6.1. Special Analytical Solution When $\alpha = 2\,(9 - 8\,\gamma)^{-\frac{1}{2}}$

[28] Before examining general solutions to equation (9), we note that there is a special analytical solution

$$Z = \frac{1}{4}(9 - 8\gamma)V^2. \tag{15}$$

This curve is a parabola that we call $\mathcal{P}$; this solution corresponds to a Froude number $Fr = \alpha = 2(9 - 8\gamma)^{-\frac{1}{2}}$. As shown in Figure 3, $\mathcal{P}$ crosses the critical curves C_I and the specific curve C_J at point A_γ. Since this point is singular, the crossing is not associated with a hydraulic jump. A bit farther, the parabola once again crosses the curve C_I at point C_γ with coordinates $(2/3,\ 1 - 9\gamma/8)$, which is a regular point, implying that the solution should become discontinuous in the neighborhood of C_γ. The parabola $\mathcal{P}$ does not pass through point P, which means that the downstream boundary conditions are not satisfied. Since the integral curve crosses the critical curve C_I, solutions with discontinuous gradients (weak shock) can also be constructed and we may find a discontinuous solution that satisfies the front condition.

[29] At point A_γ (for which det $\mathbf{M}$ = det $\mathbf{N}$ = 0), the integral curve takes one path out of an infinity of paths. Since A_γ is also a node, all the curves (except for the singular curves) are tangent to a limiting curve C_A, whose equation is given in the form of a Taylor expansion

$$Z = \frac{9 - 8\gamma}{(4\gamma - 3)^2} + \left(V - \frac{2}{4\gamma - 3}\right)\frac{-16\gamma^2 - 4\delta\gamma + 24\gamma + 9\delta - 9}{2(4\gamma - 3)(4\delta\gamma - 4\gamma - 2\delta + 3)} + O\left(V^2\right). \tag{16}$$

This equation is obtained by applying L'Hôpital's rule to equation (9). This curve is an exceptional solution to equation (9). Note that in numerical applications, we used a power series expansion to order $O(V^6)$ that ensures accuracy to within 10^{-4} in the numerical solution. A graphical representation of C_A is given in Figure 4 (dotted line).

[30] Since P is a regular point, a single integral curve passes through it: it is the trivial solution $Z = 0$ (the V axis). The situation is sketched in Figure 4a, which is a close-up of Figure 3: in this example ($\gamma = 1.05$), no integral curve except for the trivial solution $Z = 0$ passes through point P. We conclude that there is no way of joining A_γ and P when $\gamma \neq 1$ by following pieces of integral curves representing regular solutions to equation (9). The exceptional curve C_A can, however, pass through P when $\gamma = 1$; for $\gamma \neq 1$, this limiting curve does not pass through P. In that case, we can construct a solution with a weak shock at A_1 and composed of two branches: one goes from S to A_1, while the other connects A_1 to P, as shown in Figure 4b.

6.2. Numerical Solution When $\alpha \neq 2(9 - 8\gamma)^{-\frac{1}{2}}$

[31] The solution can be found by solving equation (9) numerically. This can be done by selecting a pair of points (V_S, Z_S) standing for the source point and such that $Z_S = \alpha^{-2} V_S^2$; usually, taking V_S of the order of 10^4 ensures accuracy

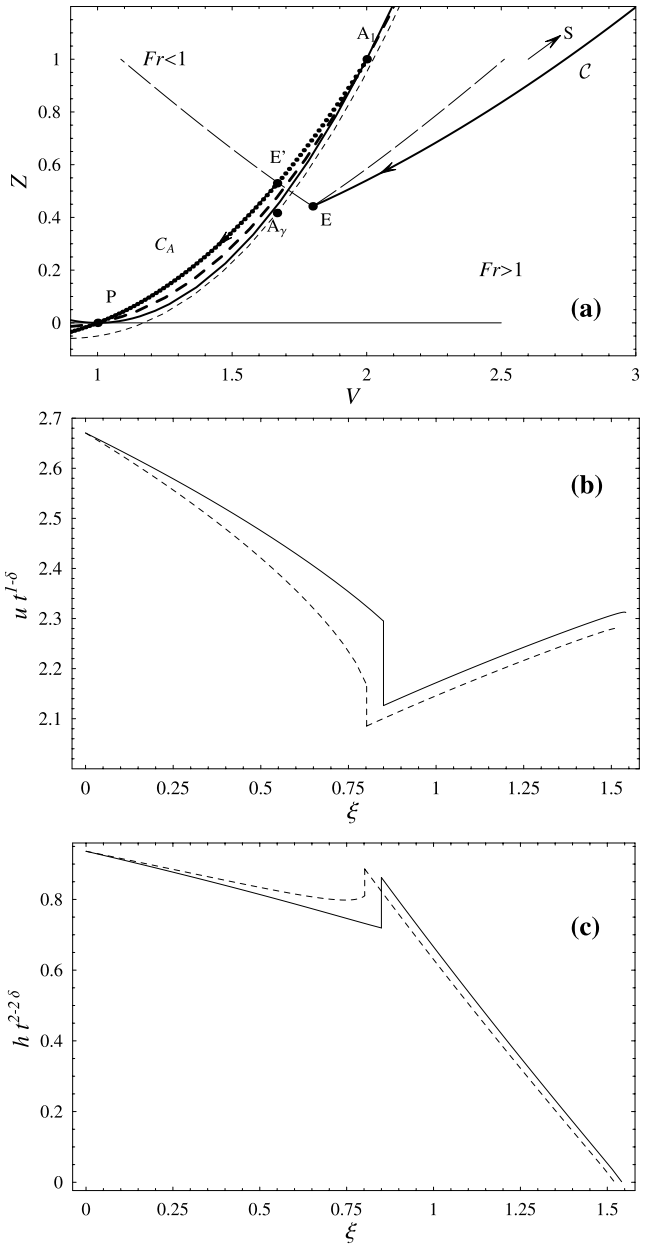

Figure 5. (a) Phase plane in the vicinity of A_γ: the specific curves C_I (solid line), C_J (dashed line), $\mathcal{P}$ (dotted line) are reported. The critical point A_γ is plotted together with the front P. The long-dashed lines represent the shock curves emanating from point E. (b) Velocity variation with ξ: the solution to the Saint-Venant equations for $\gamma = 1.05$ (solid line) is compared with the solution related to the case $\gamma = 1$ (dashed line). (c) Flow depth variation with ξ (same legend as in Figure 5b). Computations are made for $n = 5/2$, $\alpha = 2.76$, $A = 1$, and $\gamma = 1.05$ ($\beta = (nA/\alpha)^{2/3} = 0.936$).

to within 10^{-3}. The ordinary differential equation (9) is then solved using standard techniques. When coming closer to the critical curve C_I, the numerical solution starts to diverge: a discontinuous solution (strong shock) must be envisaged. The curve $\mathcal{C}$ is made up of a continuous path on either side of C_I, while the endpoints of these pieces are linked together by the shock conditions (13)–(14).

[32] We refer to point E (V_E, Z_E) as the point at which the shock occurs. First, note that it is not possible to directly relate P and E using the shock conditions (13)–(14) because a hydraulic jump cannot form between a dry bed and the current. Second, since no regular solution except the trivial solution $Z = 0$ passes through P, there is no other way of joining the subcritical and supercritical branches of $\mathcal{C}$ since the subcritical branch does not exist.

[33] Since there is no regular solution linking points P and S, we must find another way of constructing the solution. A reasonable assumption is to consider that in the vicinity of the front, the Boussinesq coefficient drops to unity, which ensures that we can find a nontrivial integral path passing through P: the limiting curve C_A, as shown in Figure 4b, is the only one passing through P except for the trivial solution $Z = 0$. We construct the solution as follows.

[34] At point E, the flow undergoes a shock: in the phase plane, this implies that there must be a shock curve mapping point E onto another point of the limiting curve C_A that we refer to as point E′. This situation is depicted in Figure 5a. On Figure 5a, we have plotted the two shock curves (long-dashed curve) emanating from E using equations (13)–(14) together with points A_γ and E′; the only physically admissible shock curve is that corresponding to a flow depth increase and a velocity decrease to ensure energy dissipation. Between E′ and P, the integral path follows the limiting curve C_A. We can now compute the solution.

[35] To determine $V(\xi)$ and $H(\xi)$, we first integrate equation (9) to obtain the relation $Z(V)$; then using equation (12), we obtain an equation in the form

$$\xi_E = \xi_S \exp\left(-\int_E^S \frac{I(V,Z(V))}{G(V,Z(V))}\,dV\right), \tag{17}$$

which allows us to compute the coordinates of point E. Taking into account the asymptotic behavior when $\xi \to 0$ given by equation (7), we can get rid of the terms representing the behavior close to the source in order to obtain a closed form for the coordinates of E. Note that when $\alpha = 2(9 - 8\gamma)^{-\frac{1}{2}}$, this computation can be done analytically

$$\xi_E = \left(\frac{2V_E\delta - 2}{3\delta}\right)^{\delta-1} \frac{\alpha\sqrt{\beta}}{\delta} V_E^\delta.$$

The path E′ → P must also be integrated numerically. To locate the position of E along the integral path, we used the trial and error procedure, as specified in Section 5. On the integral path coming from the source point, we first guess the position of point E in the phase plane V–Z. We deduce the position of E′ by seeking the intersection point between the proper shock curve and the limiting curve C_A, then we compute the relations $V(\xi)$ by solving equation (12) numerically on either piece of the solution. The volume of the current is then computed by integrating $\int_0^{\xi_f} \xi^2 Z(\xi) d\xi$ and comparing it with the expected value $A\delta^{-2}$ (see equation (8)). The position of E is then varied until the computed and expected total volumes coincide.

[36] For instance, we took the same values as those used in the numerical applications done by *Gratton and Vigo*

[1994, Figure 5]: $n = 5/2$, $\alpha = 2.76$, $A = 1$ (i.e., $\beta = 0.936$). Figure 6 shows us how the current volume varies with V_E and makes it possible to accurately locate the proper value of E. On integrating equation (17), we found $\xi_E = 0.850$, which led to $\xi_P = 1.541$. Note that in this particular numerical application, the method of constructing the solution proposed by *Gratton and Vigo* [1994] failed: indeed, the conjugate curve did not cross the integral path.

7. Similarity Solution for $\gamma = 1$

[37] We are now interested in determining the solution to equation (9) in the usual case for the Saint-Venant equations, where the Boussinesq coefficient is set equal to unity. The resulting integral path in the phase plane continues to evolve in the first quadrant ($V \geq 0$, $Z \geq 0$) and must satisfy the boundary conditions (6)–(8).

[38] The method is the same as that detailed in section 6.2. In order to evaluate the effect of γ, we report the solutions to equation (9) for $\gamma = 1$ (dashed line) and $\gamma = 1.05$ (solid line) on the same plot (see Figures 5b and 5c). There are minute differences in the numerical results. We found $\xi_E = 0.802$ and $\xi_P = 1.5120$. As shown by Figures 5b and 5c, the relative deviation in the curves $\bar{u}(\xi)$ and $h(\xi)$ are slight.

[39] We also used the method proposed by *Gratton and Vigo* [1994]. We imposed a very small flow depth at the front $Z = \kappa$ (i.e., a Froude number at the front $Fr_f = \kappa^{-1/2}$). With $\kappa = 10^{-4}$, we found $\xi_E = 0.802$ and $\xi_P = 1.522$. We checked the reliability of this solution by computing the surge volume and found an error of -0.27%. This error may be considered to be small, but it is far beyond numerical uncertainty in our computations. We failed to find any reason for this error, which was almost systematic in most numerical simulations.

8. Discussion

[40] A striking feature of our results is that the head of the surge is wedge shaped with an acute angle. This wedge structure has been observed in experimental realizations of gravity currents in tanks. Different examples drawn from various flow conditions in the laboratory and in nature clearly demonstrate the existence of wedge-like fronts contrasting with the Benjamin assumption. For instance, in the experiments conducted by *Simpson* [1972; see also *Simpson*, 1997], the development of the flow patterns was made visible by using a blend of dense fluid and fine aluminum particles: a stretching vortex occupying the tip region was clearly observed at the leading edge and produced an intense roll-up of fine aluminum particles, which makes it possible to visualize the streamlines and the two vortices; in the upper part of the head, a counterclockwise rotating vortex occurred. The free surface close to the front was clearly a straight line. At the junction between the head and the body, there was a sudden decrease in the flow depth. This flow structure is very close to the one exhibited by the Saint-Venant equations in our numerical applications. The shape of the front is, to some extent, very surprising because laboratory experiments revealed that the tip region is characterized by a significant vorticity.

[41] The results presented in this paper are borne out by experimental realizations of the flows. In particular, *Maxworthy* [1983] conducted experiments on two-dimensional gravity currents inside a horizontal tank, with variable inflow at the inlet. By imposing a power law inflow rate in the form $q \propto t^{n-1}$, he observed that the total length of the current varies as $t^{\frac{1}{3}(n+2)}$ in line with the scaling found here. For $n = \frac{7}{4}$, he reported the spreading rate of the front, but since he did not specify the boundary conditions (Froude number, initial flow depth), a direct comparison with his data was not possible.

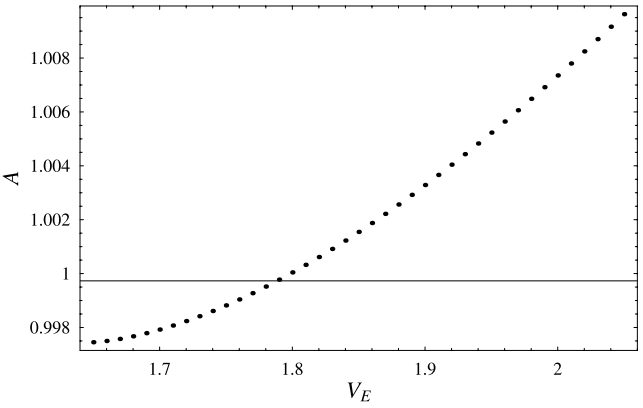

Figure 6. Variation in the current volume as a function of the position of E: the dots represent the numerical simulations, while the horizontal solid line stands for the expected value given by equation (8). Computation is made for $n = 5/2$, $\alpha = 2.76$, $A = 1$, and $\gamma = 1.05$.

[42] Another remarkable result of this investigation is that it was not possible to construct a solution when $\gamma > 1$ everywhere, whereas if we assumed that the hydraulic jump modified the velocity profile and the Boussinesq coefficient γ dropped to unity within the head, we were able to construct a piecewise continuous solution. The method proposed by *Gratton and Vigo* [1994] encountered similar difficulties since it was not possible to find numerical solutions when $\gamma > 1$. This clearly shows that minute changes in the value of γ markedly affect the structure of the solutions to the Saint-Venant equations, whereas there were few changes in the front position. An increase in γ by 5% caused a 2% increase in x_f. In their investigation of the dam break problem, *Hogg and Pritchard* [2004] arrived at the same conclusion: if $\gamma > 1$ everywhere, the solution close to the front departs significantly from the Ritter solution since the flow depth never vanished. To enforce a zero flow depth at the front, the Boussinesq coefficient must drop to unity or one must account for energy dissipation within the tip region by adding a bottom frictional force [*Hogg and Pritchard*, 2004; *Montgomery and Moodie*, 2001]. Physically, this condition on γ within the head can be understood in noting that the vortices observed experimentally contribute to making the vertical velocity profile more uniform.

9. Conclusion

[43] The goal of this paper was to find similarity solutions to the Saint-Venant (shallow water) equations when the boundary conditions at the front impose a zero flow depth, i.e., for non-Boussinesq flows for which the resisting effects of the surrounding fluid are negligible. The solutions to the

Saint-Venant equations were constructed by making use of the phase plane formalism and seeking similarity forms in a way similar to earlier investigations [*Grundy and Rottman*, 1986; *Gratton and Vigo*, 1994].

[44] When there is shear in the vertical velocity profile (i.e., Boussinesq coefficient in excess of unity), it was not possible to find a physically admissible solution for the tip region because the downstream boundary condition cannot be satisfied. Assuming that the velocity profile becomes uniform close to the front makes it possible to construct a physically admissible solution. In that case, the front is wedge shaped, with a straight free surface. Field observations and laboratory experiments are in agreement with this result.

[45] An important point that does not seem to be noted in the earlier investigations is that the integral path representing the behavior of the solution close to the front is an exceptional solution to the Saint-Venant equations, which cannot be derived by standard techniques. This topological structure of the similarity solutions in the front vicinity requires that a specific numerical method be used to compute accurate solutions to Saint-Venant equations and explains why the current numerical methods fail to accurately predict the behavior close to the front.

[46] **Acknowledgments.** The work presented here was supported by the Swiss National Science Foundation under grant 200021-105193, the competence center in Mobile Information and Communication Systems (a center supported by the Swiss National Science Foundation under grant 5005-67322), and specific funds provided by EPFL (Vice-présidence à la recherche). The authors thank E. Daly for the careful reading of the paper and constructive remarks.

References

Ancey, C. (2004), Powder-snow avalanches: Approximation as non-Boussinesq clouds with a Richardson number-dependent entrainment function, *J. Geophys. Res.*, *109*, F01005, doi:10.1029/2003JF000052.

Chanson, H. (2004), *The Hydraulics of Open Channel Flow: An Introduction*, 2nd ed., Elsevier, New York.

Daly, E., and A. Porporato (2004), Similarity solutions of nonlinear diffusion problems related to the mathematical hydraulics and the Fokker-Planck equation, *Phys. Rev. E*, *70*, 056303.

Gratton, J. (1991), Similarity and self similarity in fluid dynamics, *Fundam. Cosmic Phys.*, *15*, 1–106.

Gratton, J., and C. Vigo (1994), Self-similar gravity currents with variable inflow revisited: Plane currents, *J. Fluid Mech.*, *258*, 77–104.

Grundy, R., and J. Rottman (1985), The approach to self-similarity of the solutions of the shallow-water equations representing gravity-current releases, *J. Fluid Mech.*, *156*, 39–53.

Grundy, R., and J. Rottman (1986), Self-similar solutions of the shallow-water equations representing gravity currents with variable inflow, *J. Fluid Mech.*, *169*, 337–351.

Hogg, A., and D. Pritchard (2004), The effects of hydraulic resistance on dam-break and other shallow inertial flows, *J. Fluid Mech.*, *501*, 179–212.

Hogg, A., and A. Woods (2001), The transition from inertia- to bottom-drag-dominated motion of turbulent gravity current, *J. Fluid Mech.*, *449*, 201–224.

Huang, X., and M. Garcìa (1998), A Herschel-Bulkley model for mud flow down a slope, *J. Fluid Mech.*, *374*, 305–333.

Iverson, R., and R. Denlinger (2001), Flow of variably fluidized granular masses across three-dimensional terrain: 1. Coulomb mixture theory, *J. Geophys. Res.*, *106*, 537–552.

LeVeque, R. (2002), *Finite Volume Methods for Hyperbolic Problems*, Cambridge Univ. Press, New York.

Maxworthy, T. (1983), Gravity currents with variable inflow, *J. Fluid Mech.*, *128*, 247–257.

Montgomery, P., and T. Moodie (2001), Jump conditions for hyperbolic systems of forced conservation laws with an application to gravity currents, *Stud. Appl. Math.*, *106*, 367–392.

Parker, G., Y. Fukushima, and H. Pantin (1986), Self-accelerating turbidity currents, *J. Fluid Mech.*, *171*, 145–181.

Ritter, A. (1892), Die Fortpflanzung der Wasserwellen, *Z. Ver. Dtsch. Ing.*, *36*(33), 947–954.

Rottman, J., and J. Simpson (1983), Gravity currents produced by instantaneous releases of a heavy fluid in a rectangular channel, *J. Fluid Mech.*, *135*, 95–110.

Ruo, A., and F. Chen (2004), A similarity transformation for inviscid non-Boussinesq gravity currents, *Acta Mech.*, *173*, 33–40.

Savage, S., and K. Hutter (1989), The motion of a finite mass of granular material down a rough incline, *J. Fluid Mech.*, *199*, 177–215.

Simpson, J. (1972), Effects of a lower boundary on the head of a gravity current, *J. Fluid Mech.*, *53*, 759–768.

Simpson, J. (1997), *Gravity Currents in the Environment and the Laboratory*, Cambridge Univ. Press, New York.

Stoker, J. (1957), *Water Waves*, Wiley-Interscience, Hoboken, N. J.

Whitham, G. (1974), *Linear and Nonlinear Waves*, John Wiley, Hoboken, N. J.

C. Ancey, S. Cochard, M. Rentschler, and S. Wiederseiner, School of Architecture, Civil and Environmental Engineering, École Polytechnique Fédérale de Lausanne, CH-1015 Lausanne, Switzerland. (christophe.ancey@epfl.ch)